Enhanced oxygen reduction reaction stability on platinum nanoparticles photo-deposited onto oxide-carbon composites

Luis Alberto Estudillo-Wong, Yun Luo, Jesús Adrián Díaz-Real, Nicolas Alonso-Vante *

IC2MP, UMR-CNRS 7285, Université de Poitiers, 4 rue Michel Brunet, F-86073 Poitiers, France

ABSTRACT

Oxide-Carbon composites (TiO_2-C) and yttrium-doped TiO_2-C ($Y:TiO_2$-C), synthesized via sol-gel route, were used as supports to photo-deposit platinum nanoparticles (Pt NPs). The physical-chemical properties of these materials were investigated by Transmission Electron Microscopy (TEM) and X-ray diffraction (XRD). The TEM images showed that Pt NPs were agglomerated and deposited onto oxide sites of the composites. Pt face-centered cubic, and TiO_2 Anatase phases were identified on both Pt/TiO_2-C and $Pt/Y:TiO_2$-C samples. The particle size, stacking fault and micro-strain of Pt NPs were estimated by Williamson-Hall method. Compared with Pt/TiO_2-C, similar stacking faults as well as increased crystallite sizes and micro-strain values could be observed for $Pt/Y:TiO_2$-C sample, indicating a minimum impact of the rare earth element on Pt. Pt/C was prepared by the same method, and used as a reference catalyst. The strong-metal/support interaction (SMSI) effect induced by the photo-deposition method, in Pt/TiO_2-C and $Pt/Y:TiO_2$-C samples, was probed by CO-stripping, and associated to the enhanced stability toward the oxygen reduction reaction (ORR) in acid medium.

© 2016 Elsevier B.V. All rights reserved.

1. Introduction

Although the proton exchange membrane fuel cells (PEMFCs) is one of the most promising candidates in clean energy sources, the cathode catalyst issue is still a great challenge for its large-scale commercialization because of the following reasons: (1) the low efficiency of the electrochemical reaction at the catalytic centre [1,2]; (2) the degradation of the carbon black, used as a popular support, a major cause of loss of the cell performance during long-term operation [3]. Since oxygen reduction reaction (ORR) at the cathode is more difficult than the oxidation of fuels (*i.e.* hydrogen, formic acid) at the anode, it is the key to improve the efficiency of PEMFCs. Although Pt-based materials are proven as the best electrocatalyst, the cathodic performance toward durability in fuel cells is still insufficient [4]. Therefore, a number of alternative electrocatalysts has been proposed to enhance the ORR kinetics on Pt-based catalysts, such as: $Pt-Ln_2O_3/C$ (Ln = Y and Gd) [5], Pt-M/C (M = Fe, Co and Cr) [6], Pt-Pd alloy nanoflowers [7], as well as their stability on carbon supports [8,9]. Regarding the deterioration of ORR activity, it was reported that the agglomeration of nanoparticles derived from electrochemical corrosion of supports lead to the

degradation of electrocatalysts in acid and alkaline environments [10,11]. Such an agglomeration of Pt nanoparticles, induced by the corrosion of the support, can be actually reduced by applying a corrosion-resistant support [12–14]. The oxide-carbon composite is a good candidate since Pt electronic modification can be induced, *via* strong metal-support interaction (SMSI) [12,14–16] and finally improving the ORR activity and/or stability. Additionally, supports with suitable porosity (mesoporous material), with high conductivity, high surface area, and resistant to oxidation will favor the catalytic performance of Pt active site towards ORR [3].

Conversely, the photo-deposition method has been exploited to deposit metals nanoparticles on semiconductor materials [13,17–20]. Titanium dioxide (TiO_2, Anatase phase) was selected to prepare oxide-carbon composite as support for nanoparticles. It is a large band-gap (E_g = 3.2 eV) semiconductor, that plays an important role in photocatalysis [21,22] allowing for the photo-deposition of metal NPs, *e.g.* Pt [13] via UV-irradiation. Its photoactivity can be tuned depending on the nature of the dopants, *e.g.* transition metals [23–26] or rare earth (RE) elements such as Cerium (Ce) [27] and Yttrium (Y) [28]. The $Y:TiO_2$ material presents a reasonable photoactivity to be applied for the degradation of organic molecules. Therefore, RE-doped TiO_2 (Anatase phase) should be a promising support for Pt NPs. Herein, we report Y-doped TiO_2 and carbon composite ($Y:TiO_2$-C), prepared via sol-gel route, applied as supporting materials for Pt NPs. This latter was photo-deposited mainly onto

the oxide sites to prepare Pt/Y:TiO$_2$-C catalyst. The electro-catalytic performance towards ORR kinetics, and stability in acid medium were investigated and compared to Pt/TiO$_2$-C and Pt/C catalyst, synthesized by the same method.

2. Experimental

2.1. Synthesis of Y:TiO$_2$-C and TiO$_2$-C composites

The Y-doped TiO$_2$-C (Y:TiO$_2$-C) composites were prepared by mixing carbon Vulcan (XC-72) with titanium isopropoxide and YCl$_3$ in isopropanol solvent on ice/water bath (*ca.* 4 °C) [13]. To synthesize 20 wt.% Y:TiO$_2$, 31.4 mg YCl$_3$ (99.9%, Alfa-Aesar) was dissolved with isopropanol (99.9%, Alfa-Aesar) also on ice/water bath for 4 h. A volume of 189.1 μL of titanium isopropoxide (TIP, 99.9%, Sigma-Aldrich) was added to have a ratio of Ti/Y = 7 mol/3 mol at *ca.* 4 °C and mixed further for 16 h. Afterwards, 200 mg of carbon (preheated at 400 °C under N$_2$ for 4 h) was incorporated in the suspension and stirred for 1 more hour. One mL of ultra-pure water (18.2 MΩ-cm, MilliQ) was added to hydrolyze TIP and produce Y:TiO$_2$ further stirred for 4 h in ice/water bath. Subsequently, the isopropanol solvent was evaporated at 100 °C. The as-prepared material was rinsed by ultra-pure water and then dried at 60 °C, overnight. Finally, the sample was heat-treated at 400 °C for 1 h under nitrogen (99.99%, Air Liquide) atmosphere. Same procedure was carried out for the synthesis of TiO$_2$-C (20 wt.% TiO$_2$). The synthesis of the oxides Y:TiO$_2$ and TiO$_2$ was also done.

Preparation of Pt/TiO$_2$-C and Pt/Y:TiO$_2$-C via photo-deposition method (PD Method). Pt NPs were deposited by irradiation as follows. To produce 20 wt.% Pt, 25 mL deionized water with 100 mg of Y:TiO$_2$-C or TiO$_2$-C composites was mixed ultrasonically for 20 min in a photo-reactor [29]. The system was saturated with nitrogen for another 20 min. Then, 6 mL of isopropanol solution containing 66.4 mg of H$_2$PtCl$_6$ + 6H$_2$O (99.9%, Alfa-Aesar) was added into the photo-reactor and kept under constant stirring for 3 h. For reference purposes, Pt NPs (20 wt.% Pt) supported on C and TiO$_2$ were prepared with the same protocol. Carbon-supported Pt NPs (20 wt.% Pt) was also prepared by carbonyl chemical route (CCR) and heat-treated at 300 °C for 3 h in nitrogen atmosphere. The source of ultraviolet (UV–vis) radiation used for the experiments was a Xe lamp (159 W) provided with a water filter.

2.2. (Photo)-electrochemical and electrochemical measurement

The (photo)-electrochemical measurements were performed using a potentiostat in a three-electrode standard electrochemical cell (EC) and photo-electrochemical cell (PEC). For EC, a carbon rod and reversible hydrogen electrode (RHE) were used as a counter and reference electrode, respectively. A gold disk electrode with 3 mm (0.07 cm^2), polished to a mirror-like finish with a 0.05-μm alumina suspension before each experiment, was used for the catalyst ink deposit. The latter was prepared by dispersing 5 mg of electrocatalyst in 710 μL of water-isopropanol solution (3:1 vol.) and 40 μL Nafion® (5 wt.% Nafion®). The suspension was mixed and ultrasonicated for 1 h on a water bath at room temperature. A drop of 3 μL of the ink was deposited onto gold surface of a rotating disk electrode (RDE) and dried at a rotating rate of 300 rpm in air for at least 30 min. Prior to electrochemical measurements, in order to stabilize the current-potential signals, the working electrode was activated in 0.1 M HClO$_4$ solution with 20 potential CVs cycles from 0.05 to 1.2 V/RHE at scan rate of 50 mV s^{-1}. Before CO-stripping, two CVs cycles from 0.05 to 1.2 V/RHE was performed at 5 mV s^{-1} to assure the steady-state conditions. CO was adsorbed at 0.1 V/RHE in CO-saturated electrolyte (99% CO) for 3 min, and further purged for 30 more min with nitrogen. Two potential cycles

from 0.05 to 1.2 V/RHE was recorded at v = 5 mV s^{-1}. The ORR polarization curves were recorded at scan rate of 5 mV s^{-1} in O$_2$ (99.99%, Air Liquide) saturated electrolyte, with rotating speeds of 400, 900, 1600 and 2500 rpm. For the accelerated stability test (AST) analyses, the working electrode was cycled at 50 mV s^{-1} from 0.6 to 1.0 or to 1.2 V/RHE in N$_2$-saturated electrolyte. After each 500 potential cycles, the working electrode was activated at 50 mV s^{-1} in N$_2$-saturated electrolyte.

For photo-electrochemistry, the working photo-electrodes were prepared by spin coating (at 3000 rpm) using a suspension of the oxides in 15 mg mL^{-1} of ethanol (99.9%, Alfa-Aesar) and deposited on SnO$_2$:F (FTO) support of 0.35 cm^2. After ejection and evaporation of the solvent, a porous adhering thin film was formed. The samples were sintered afterwards, in air at 450 °C for 1 h. The photoelectrochemical cell (PEC) was provided with a quartz window and was placed on an optical table on a support that allowed the displacement of all the system in X-, Y- and Z-directions. The measurement was carried out under UV–vis illumination and in the darkness. The UV–vis source of light was from a Xenon lamp, Spectral products ASB-XE-175. Current-potential curves were performed in N$_2$-saturated electrolyte, from 0.05 to 1 V/RHE.

The electrical conductivity of powders was determined using a homemade four-probe cell [30] *via* impedance spectroscopy. The system consists of a hollow cylinder constructed with a Plexiglas material, in which two metallic cylinders served as electrodes. Two wires penetrating *ca.* 1 mm into the sample chamber, were assembled. The sample chamber was submitted to 25 lb in^{-2} (172.4 kPa).

2.3. X-ray diffraction, TEM and ICP analysis

The nanoparticle sizes for all samples were evaluated by TEM on a JEOL microscope (JEM-2001). The samples were dispersed in ethanol and then a drop of such solution was placed on a copper grid covered by carbon film and the solvent was evaporated. For all electrocatalysts, the diameter of particles from TEM images was evaluated by the free ImageJ software. Particle-size-distribution histograms were done by counting 30 particles in different TEM images. The stoichiometric composition of all electrocatalysts was analyzed by inductively coupled plasma optical emission spectrometry (ICP-OES, Optima 2000 DV, PerkinElmer). The powder X-ray diffraction (*p*XRD) was performed on an Empyrean Panalytical X-ray diffractometer using Cu-Kα radiation (λ = 0.15406 nm). The *p*XRD patterns were obtained, using high resolution, with step-scanning mode, slit at 1/16°, and counting time of 240 s/0.05° in the range of 20°–95°. Using the Joint Committee on Powder Diffraction Standard International Centre for Diffraction Data (JCPD-ICDD), the structural phase in *p*XRD pattern was identified. The instrumental broadening was corrected by the standard pattern of LaB$_6$. Prior to analysis of pXRD patterns of Pt-based catalysts, XRD pattern of support was used to calibrate the background contribution. The lattice parameter, *a*, of catalyst was estimated using Eq. (1) [31].

$$2\theta_{hkl} = 2\sin^{-1}\left(\frac{\lambda}{2a}\sqrt{h^2 + k^2 + l^2}\right) \tag{1}$$

where λ = Cu-Kα radiation, θ angle Bragg diffraction in radians, and *hkl* Miller indices. In PD method, each Bragg diffraction peak was fitted with Pearson VII function. In Pt/C CCR, Pearson VII and Pseudo-Voigt functions were used for deconvolution of the contribution on each Bragg diffraction peak. These functions aid to obtain the parameters such as *a*, θ_{hkl} and full-width at half-maximum (FWHM, β$_f$), Eqs. (2)–(6).

$$I_C = \frac{I_{hkl}}{\left(1 + \kappa * \Delta\theta^2\right)^m} \tag{2}$$

$$\kappa = \frac{4\left(2^{1/m} - 1\right)}{\beta_f^2} \tag{3}$$

$$I_C = I_{hkl}\left\{(1-m) * \exp\left(-\ln 2 * 4\kappa_I^2\right) + \frac{m}{1+4\kappa_I^2}\right\} \tag{4}$$

$$\kappa_I = \frac{\Delta 2\theta}{\beta_f} \tag{5}$$

$$\Delta 2\theta = 2\theta_i - 2\theta_{hkl} \tag{6}$$

where I_C is the calculated profile intensity of a data point i in Eq. (6), I_{hkl} is the peak height. The κ, κ_I, θ_{hkl}, a, β_f, and m constants were extracted by Leverberg-Marquardt algorithm implemented in Eq. (7) using Fityk (free software).

$$F\left(\kappa, \kappa_I, \theta_{hkl}, a, \beta_f\right) = \Sigma_i f_i\left(I_{exp} - I_C\right) \tag{7}$$

All Pt diffraction peaks were used to calculate the mean crystallite size according to the line-broadening analysis and Williamson-Hall plot [32].

3. Results and discussion

3.1. Physical-chemical characterization

3.1.1. Morphology and mass analysis

Fig. 1 shows the TEM images for Pt/C, Fig. 1(A, B), Pt/TiO$_2$-C, Fig. 1(D, E), and Pt/Y:TiO$_2$-C, Fig. 1(G, H). The particle size histograms of Pt were obtained by measuring the diameter of *ca.* 30 particles in different TEM images, Fig. 1(C, F, I). The mean particle size of Pt NPs are 16 ± 3 nm, 7.1 ± 1 nm, and 19 ± 5 nm, respectively, for Pt/C, Pt/TiO$_2$-C and Pt/Y:TiO$_2$-C samples. Thus, Pt particle size in Pt/Y:TiO$_2$-C is similar to that in Pt/C sample, whereas a diameter of 7.1 ± 1 nm was found for Pt/TiO$_2$-C sample. Fig. 1(B, E, H) shows the TEM images at high-resolution in different zones. A fast Fourier transform (FFT) analysis, insets of Fig. 1B, reveals that Pt particles grow on [100] and [110] directions on Carbon. The same growth direction of Pt NPs appears onto TiO$_2$-C and Y:TiO$_2$-C composites (*cf.* insets in Fig. 1(E, H)). One can thus conclude that Pt NPs present same facets on all the samples. Besides, as described in previous work, Pt NPs could be deposited outside semiconducting oxide site regions, i.e., onto graphitic domains of carbon [33]. One can thus deduce that Pt NPs are agglomerated on oxides, Fig. 1(E, H), and on sp^2 [33] domains of the carbon black [12,34]. The ICP-OES analysis, summarized in Table 1, confirms that the mass loading of platinum and TiO$_2$ is close to the nominal value. However, yttrium is present in a lower amount. The reason could be that Y is not completely "dissolved" in TiO$_2$ phase, even though the molar ratio of Ti/Y was fixed as 7/3 in the synthesis, *cf.* Supplementary Information (SI). This is the reason why we describe this material as Y-doped Titania (Y:TiO$_2$), further supported by results generated from XRD and photo-electrochemistry discussed below.

3.1.2. X-ray diffraction analysis

The *p*XRD corresponding to Pt/C by CCR, Pt/C, Pt/TiO$_2$-C and Pt/Y:TiO$_2$-C by PD are shown in Fig. 2. The X-ray diffraction patterns in PD were fitted using a Pearson VII function. Both, Pearson VII and Pseudo-Voigt functions were used in Pt/C CCR sample. It is clear that all catalysts present five typical peaks characteristic of the face-centered cubic (*fcc*) Pt phase: Pt(1 1 1), Pt(2 0 0), Pt(2 2 0), Pt(3 1 1) and Pt(2 2 2) planes. The presence of the Anatase phase of TiO$_2$ can be identified in Pt/TiO$_2$-C and Pt/Y:TiO$_2$-C samples. Information concerning the microstructure of samples can be estimated from the fitted patterns presented in Fig. 2A by using the peak broadening analysis based on Williamson-Hall plot. The values of the integral peak width ($db = \beta_f \cos(\theta)/\lambda$) were plotted against $b = 2 \sin(\theta)/\lambda$, where θ is the Bragg angle and λ the wavelength in

nanometers, *cf.* Fig. 2B. Regarding the PD samples in this figure, it can be seen that, the *db* parameter slightly depends on *b* in Pt/C sample implying that the XRD patterns is not only affected by crystalline size, but by micro-strain [5]. Additionally, it signifies that the stacking faults can be also responsible for an additional line broadening, relative to the Miller indexes [35]. Nonetheless, different phenomena can be observed on Pt/TiO$_2$-C and Pt/Y:TiO$_2$-C samples, where *db* does not apparently vary or increase with *b*.

Three different contributions to the integral line width broadening must be taken into account, namely, crystallite size, stacking fault and micro-strain. According to Eq. (8) [5,35].

$$db = \frac{k}{<d>} + \frac{V_{hkl}}{a}\alpha + 2\varepsilon b \tag{8}$$

where is the mean crystalline size, V_{hkl} is a constant depending on the miller indexes *hkl* ($V_{111} = 0.43$, $V_{200} = 1$, $V_{220} = 0.71$, $V_{311} = 0.45$ and $V_{222} = 0.43$), k is the Scherrer constant considering equal to 1, a is the lattice parameter, α is the stacking faults, and ε is the micro-strain. As a result of the best fit (open circles, Fig. 2B), the obtained values of , α, and ε are summarized in Table 1. There are clear indications that the contact between Pt and carbon is completely different using the photo-deposition method, with respect to sample synthesized *via* CCR. Indeed, one can observe that the lattice parameter was 3.9063 Å for Pt/C (PD) sample. This value is lower than those values obtained in Pt NPs synthesized by the carbonyl chemical route (3.9218 and 3.9314 Å).

Additionally, the micro-strain and stacking faults are also higher in Pt/C generated by the photo-deposition method (*cf.* Table 1). Considering these contributions, the crystallite size in Pt/C (PD) was 18.8 nm without heat-treatment. However, Pt NPs in Pt/C (CCR) show a bi-modal behavior, where the crystallite sizes were 4 and 66.7 nm (*cf.* Fig. 2B, Table 1). Thus, different phenomena in Pt/C (PD) with respect to Pt/C (CCR) might be due to the interaction with sp^2 or sp^3 domains of carbon, which could be confirmed by the CO-stripping analysis (discussed later). Therefore, these results suggest that the interaction between Pt and carbon domains is partial with the photo-deposition method as compared with Pt deposited by the carbonyl chemical route.

Besides structural analysis of Pt/C, for photo-deposition of Pt NPs, the Pt–Pt distance increases from 2.7621 to 2.7703 (2.7663) Å in Pt/C (PD) and Pt/TiO$_2$-C (Pt/Y:TiO$_2$-C), respectively. These data suggest platinum atoms from Pt NPs, is interacting in sites, preferentially onto carbon-sp^2, induced by light. However, this interaction between Pt atoms and the metal of the oxide sites leads to the formation of Pt-Ti nano-alloy [14]. No yttrium-oxide diffraction peak could be identified, and thus Y atoms most probable act as a dopant in TiO$_2$. This observation is supported by photo-electrochemistry, described in the Supplementary information. The stacking fault follows the trend: Pt/Y:TiO$_2$-C $\approx$ Pt/TiO$_2$-C > Pt/C. For micro-strain, one can find the sequence: Pt/C > Pt/Y:TiO$_2$-C > Pt/TiO$_2$-C. These results might confirm less Pt surface defects on Pt/Y:TiO$_2$-C and Pt/TiO$_2$-C samples with respect to Pt/C [5]. Finally, the crystallite size obtained on Pt/C (18.8 nm), and Pt/Y:TiO$_2$-C (19.4 nm) was similar, whereas that of Pt/TiO$_2$-C is much lower (7.5 nm). These results are in good agreement with TEM analysis. The reason why crystallite size on Pt/Y:TiO$_2$-C increased with respect to Pt/TiO$_2$-C should be related to the different surface energy of Y-doped TiO$_2$ phase [17], see below.

3.2. Photo-electrochemistry—oxide and Y-doped oxide

The photo-generated current transients curves for Y:TiO$_2$ and TiO$_2$ porous oxide films measured under UV–vis illumination are shown in Fig. 3. The experiments were carried out in 0.5 M H$_2$SO$_4$ at room temperature with a scan-rate of 5 mVs^{-1} in order to minimize capacitive contributions. On Y:TiO$_2$ linear sweep voltammetry
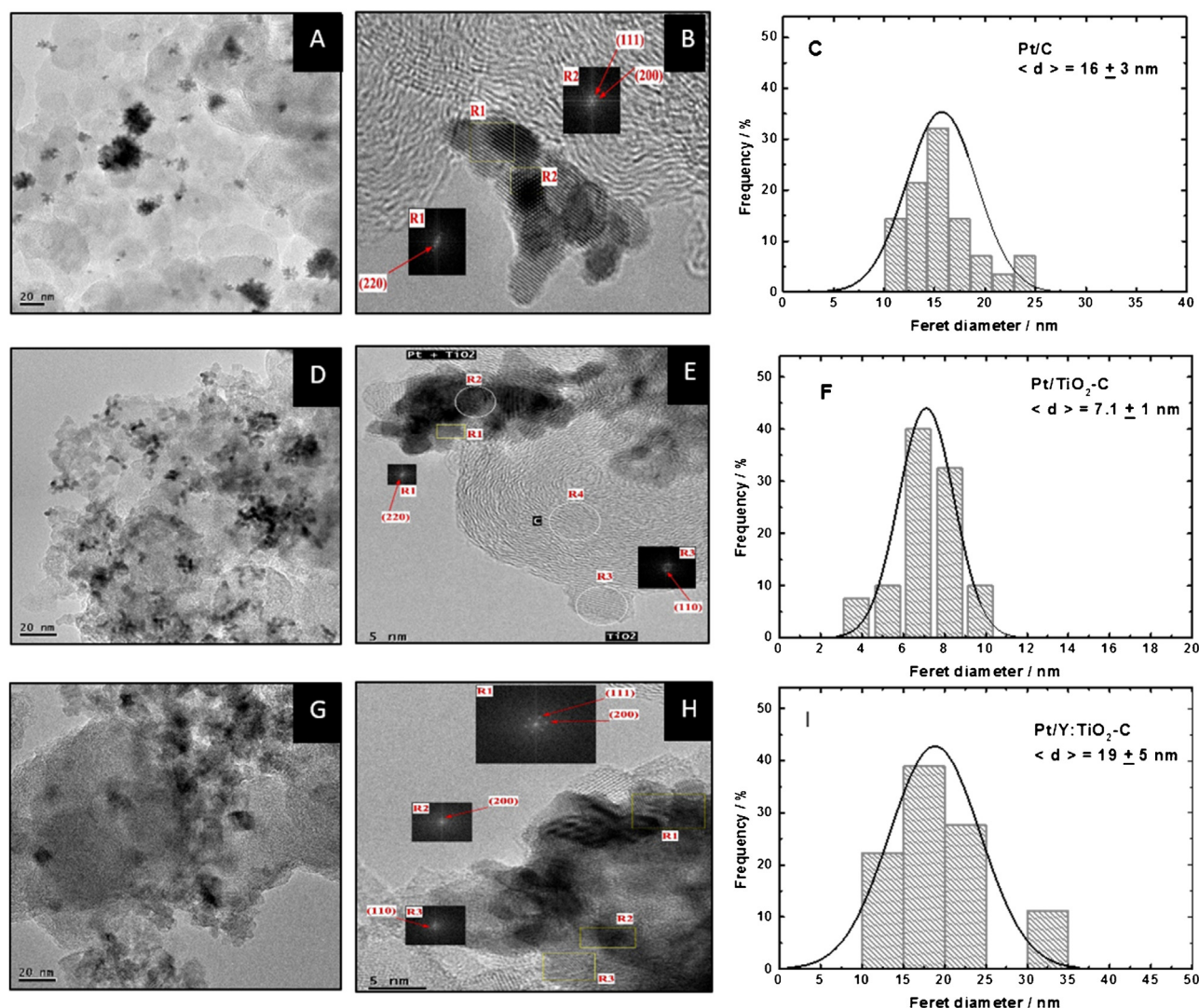
Fig. 1. TEM images and particle size histograms deduced from the TEM images for Pt/C (A, B), Pt/TiO$_2$-C (D, E) and Pt/Y:TiO$_2$-C (G, H). Insets in B, E, H, are the Fast Fourier Transform (FFT) on high-resolution images.

Table 1
Structural parameters of the obtained Pt/C, Pt/TiO$_2$-C and Pt/Y:TiO$_2$-C electrocatalysts, calculated from the XRD and TEM data.

Sample	a/Å	<d>/nmXRD(TEM)	% α	% ε	wt.% PtNominal (ICP)	wt.% TiNominal (ICP)	wt.% YNominal (ICP)
Pt/C,	[a]3.9218	[a]66.7	[a]0.04	[a]0.17	–	–	–
CCR	[b]3.9314	[b]4.0	[b]0.41	[b]0.69			
Pt/C	3.9063	18.8 (16)	0.66	0.85	20 (18.54)	–	–
Pt/TiO$_2$-C	3.9178	7.5 (7.1)	2.49	0.26	20 (18.67)	9.59 (7.69)	–
Pt/Y:TiO$_2$-C	3.9121	19.4 (19)	2.51	0.51	20 (19.07)	9.59 (8.53)	7.63 (0.14)

[a] Pseudo-voigt were used to deconvolution each Bragg diffraction peak.
[b] Pearson VII functions were used to deconvolution each Bragg diffraction peak.

(LSVs) shows that the onset potential (E$_{onset}$) occurs at 0.4 V/RHE, whereas on TiO$_2$ it takes place at a potential of ~0.07 V/RHE. It should be noted that the photocurrent density in Y:TiO$_2$ is 6-fold lower than on TiO$_2$, in this pH condition. Charge carriers recombination seems to be much more efficient in the Y-doped sample. The effective separation process of electron-hole pairs e$^-$-h$^+$ at Y:TiO$_2$ starts at more positive potentials than at TiO$_2$. The shift on the onset potential might arise by the fact that yttrium doping effect creates trap levels, favoring the increase of e$^-$-h$^+$ recombination in the band gap of TiO$_2$ [36], leading to a modified surface chemistry that leads to a shift of the conduction band and valence band energy levels. Under chopped light, at more positive applied

electrode potentials, this process is clearly contrasted at Y:TiO$_2$. This phenomenon can be understood as a metallization-like process that modifies the opto-electronic properties of the material. As consequence, the conductivity of Y:TiO$_2$ increased, as described below. Additionally, the insets in Fig. 3 contrasts the CVs behavior in darkness, in the interval potential from 0.05 to 1 V/RHE. These CVs clearly show differences between Y:TiO$_2$ and TiO$_2$. The cathodic feature at Y:TiO$_2$ centered at 0.25 V/RHE is hardly observable at TiO$_2$.

This feature has been previously attributed to the filling of mono-energetic trap states, such as grain boundaries, highly depending on the materials morphology and structure [37]. Thus
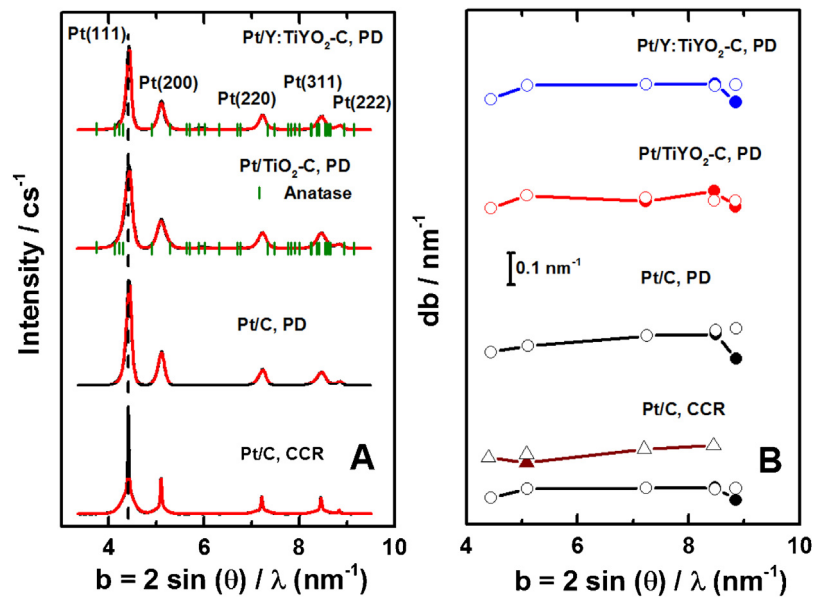
Fig. 2. (A) Corrected and fitted (red line) XRD patterns of as prepared samples Pt/C, Pt/TiO$_2$-C and Pt/Y:TiO$_2$-C. (B) Williamson-Hall plots of all samples with experimental data (full symbols) and simulated data (open symbols). (For interpretation of the references to color in this figure legend, the reader is referred to the web version of this article.).
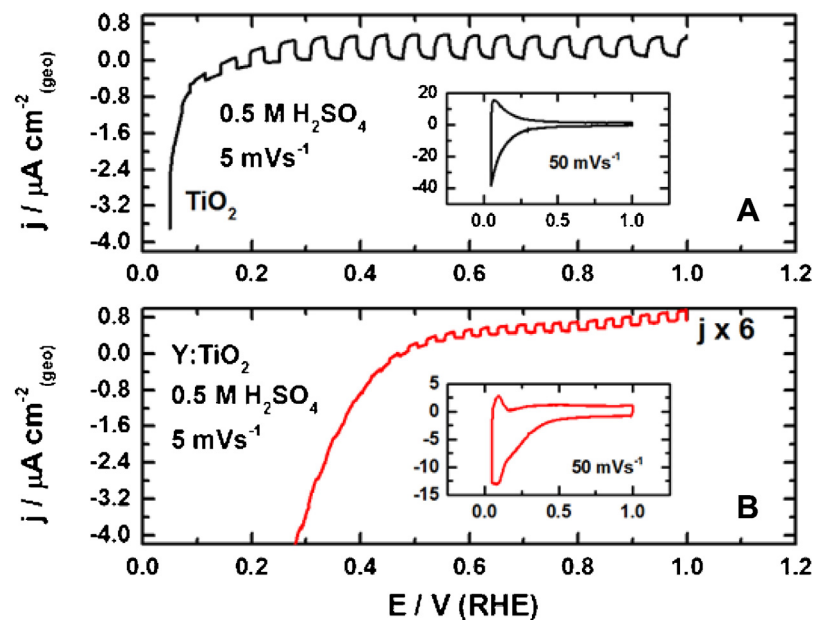

Fig. 3. The chopped light (on-off) photocurrent response at TiO$_2$ (A) and Y:TiO$_2$ (B) oxides in 0.5 M H$_2$SO$_4$ at 5 mVs^{-1}. Inset: current-potential curves (in dark) in the interval from 0.05 to 1 V/RHE at 25 °C.

indicating that this intrinsic properties in Y:TiO$_2$ has been changed with respect to TiO$_2$ and consistent with the observations in Fig. S1 [38]. The LSV curves under chopped light, in Fig. 3, can also be related to their respective CVs measured in darkness (insets, Fig. 3). The cathodic bump occurring in the cathodic sweep confirms that the trapping-detrapping kinetics govern the Y:TiO$_2$ system.

The filling of these traps should appear near the flat band potential (E_{fb}) due to a condition of electron depletion of the conduction band, accompanied by an anodic capacitive peak (centered near 0.4 V/RHE) that corresponds to the detrapping process [39]. The asymmetries of these kinetics (observable in terms of current density and E) are indicative of the difference on the rate for both processes. Since the E$_{onset}$ is associated to the position of E_{fb}, it is possible to confirm a shifting in this parameter as consequence

of the Y-doping and the photo-generation of charge carriers (at potentials below 0.25 V) [40]. The observed photo-activity, *cf.* Fig. 3, confirms that the synthesized Y:TiO$_2$ material can be used as support for photo-deposition of Pt NPs [28]. All these facts, indeed, reveal that photo-electrochemical and electrochemical properties of TiO$_2$ is modified by Y, demonstrating the doping effect of Y on TiO$_2$.

One of the main concerns for oxide and oxide-carbon composites is the conductivity [30]. In order to investigate the effect of carbon towards the conductivity (σ), this parameter was estimated for Vulcan (XC-72), TiO$_2$-C, Y:TiO$_2$-C, Y:TiO$_2$ and TiO$_2$ samples. Data of resistance were read at the lower frequency (1–1000 Hz) in the Bode plot (data not shown here). Fig. 4 summarizes these σ data for Vulcan (XC-72), TiO$_2$-C, Y:TiO$_2$-C, Y:TiO$_2$ and TiO$_2$ samples sub-
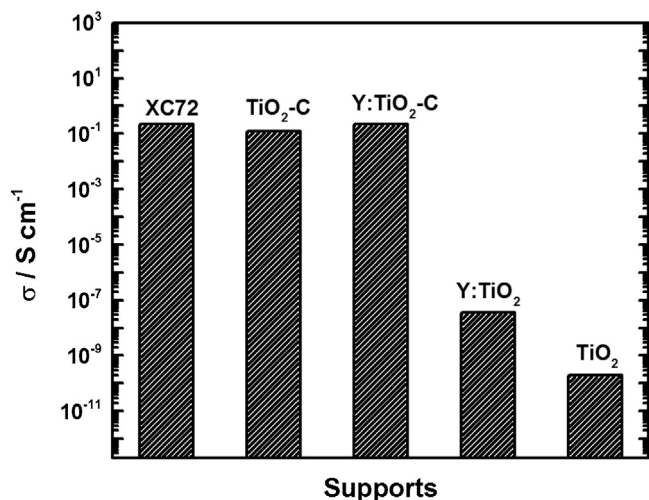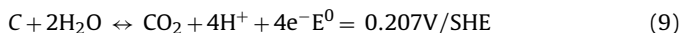
Fig. 4. Electrical conductivity σ/S cm^{-1} for XC-72, TiO$_2$-C, Y:TiO$_2$-C, Y-doped TiO$_2$ and TiO$_2$ supports submitted at 25 lb in^{-2}.

mitted to 25 lb in^{-2}. One can notice that the conductivity of TiO$_2$ increased after doping, Fig. 4. Both oxide-carbon composites, with 20 wt% oxide loading, present conductivity values close to that of Vulcan (XC-72).

3.3. Surface electrochemistry

3.3.1. Corrosion and conductivity of oxide-carbon composite

The thermodynamic carbon corrosion of carbon process is given by Eq. (9) [23,41].

$$C + 2H_2O \leftrightarrow CO_2 + 4H^+ + 4e^- \quad E^0 = 0.207\,V/SHE \quad (9)$$

The carbon corrosion is hindered kinetically and takes place at potentials >0.9 V. The corrosion of carbon kinetics, in the oxide-carbon composite, can be further hindered to some extent [34]. Prior to corrosion experiments on Vulcan (XC-72), TiO$_2$-C and Y:TiO$_2$-C composites, 20 cycles of CVs between 0.05 to 1 V/RHE at 50 mVs^{-1} were performed in 0.5 M H$_2$SO$_4$ at 25 °C to obtain stable voltammograms. The last scan (20th cycle) is shown in Fig. 5.

One can observe a decrease sequence in the capacitance current, namely, Vulcan (XC-72) (489 μC cm^{-2}$_{geo}$) $\square$ TiO$_2$-C (401 μC cm^{-2}$_{geo}$) $\square$ Y:TiO$_2$-C (323 μC cm^{-2}$_{geo}$). The insets in Fig. 5 show two LVs from 0.5 to 1.3 V/RHE at 5 mV s^{-1}. One can further notice that the corrosion potential sets on at ~1.0 V/RHE (see vertical dashed line in the inset), for all samples. It can be seen that, in the first scan (black line) on Vulcan (XC-72), the LSV reveals a shoulder centered at 1.16 V/RHE, attributed to OH$^-$ ions adsorption [41] and consequence of the oxygen evolution reaction. Therefore, the OH$^-$ ions and/or O$_2$-adsorbed, at carbon surface, might increase the carbon corrosion process [41]. This phenomenon is not observed on both TiO$_2$-C and Y:TiO$_2$-C samples, principally suggesting that the OH$^-$ ions should be adsorbed onto the oxide sites [42].

The second LSV scan (red line) shows a concomitant decrease of the current density for all samples. After this process, the CVs were again performed and the 20th cycle, depicted as red line in Fig. 5. The appearance of a current wave, centered at 0.66 V/RHE in the XC-72 support, reveals the presence of Quinone/Hydroquinone surface species [41]. This latter is more important on Vulcan (XC-72) sample than on composites, demonstrating higher corrosion without presence of oxides in the composite (cf. Fig. S2, in SI). The CO$_2$ production, Eq. (9), indirectly obtained from anodic electrical charge (from 0.4 to 0.9 V/RHE in the CVs), before and after corrosion and normalized by the value in carbon, confirmed this process. It gradually reduced as follows: Vulcan (XC-72) (36% CO$_2$) > TiO$_2$-C (24%

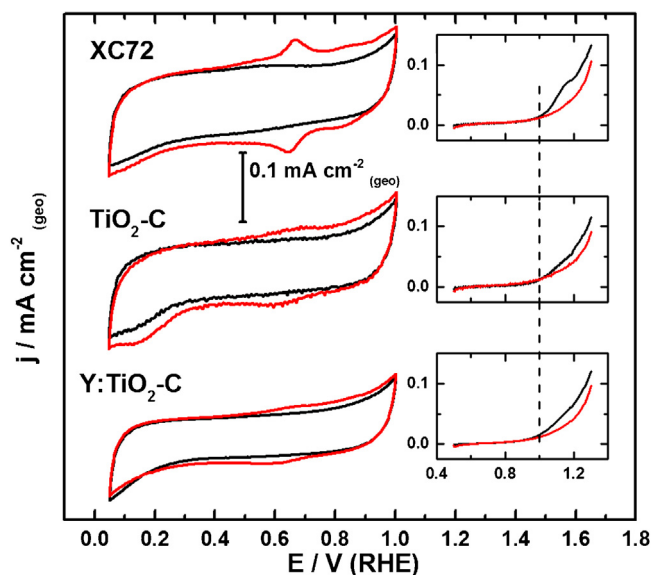**Fig. 5.** Current-potential characteristics of carbon (XC-72), TiO$_2$-C and Y:TiO$_2$-C at 25 °C in 0.5 M H$_2$SO$_4$. Prior to corrosion (black line) and after corrosion (red line). Insets: Lineal sweep voltammetry for all supports. (For interpretation of the references to color in this figure legend and text, the reader is referred to the web version of this article.)
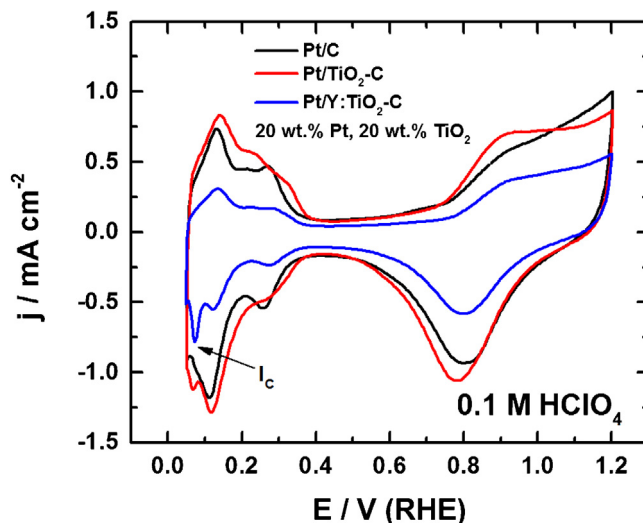

Fig. 6. Current-potential characteristic for Pt-based nanoparticles onto a gold disk in 0.1 M HClO$_4$ for Pt/C, Pt/TiO$_2$-C and Pt/Y:TiO$_2$-C at 25 °C.

CO$_2$) > Y:TiO$_2$-C (14% CO$_2$). These results, as expected, in TiO$_2$-C and Y:TiO$_2$-C composites, showed again better corrosion resistance of carbon in the composites with respect to Vulcan (XC-72) sample.

3.3.2. Hydrogen-UPD

The surface electrochemical properties of Pt NPs photodeposited onto the various supports were investigated in acid solution at room temperature. Fig. 6 depicts the j-E profiles for Pt NPs on XC-72, TiO$_2$-C and Y:TiO$_2$-C. The CV curves show the typical redox process attributed to Pt-based electrocatalyst. We can observe possible contributions of (110) and (100) sites [43], judging the hydrogen under-potential deposition (H$_{upd}$) region. One peak near 0.05 V/RHE (labelled as I$_c$ in Fig. 6) are present only on Pt/TiO$_2$-C and Pt/Y:TiO$_2$-C samples, a difference in the H$_{upd}$ with respect to that on carbon black emerges, in agreement with TEM and XRD analyses. Furthermore, the highest surface of H$_{upd}$ region obtained on Pt/TiO$_2$-C, is probably due to the particle size

Table 2
Electrochemical active surface area (ECSA) and roughness for all electrocatalyst.

Sample	ECSA m^2 g^{-1}$_{Pt}$(cm^2$_{Pt}$)	θ = ECSA$_{CO}$/ECSA$_H$	[f]Roughness
[a]Pt/C	[c]36(1.3)	1	18
[a]Pt/TiO$_2$-C	[c]42(1.6)	1	23
[a]Pt/Y:TiO$_2$-C	[c]21(0.8)	1	11
[a]Pt/TiO$_2$	[d,e]6(0.32)	2	[e]5
[b]Pt/C	[d]59(2.4)	1	33

[a] PD method.
[b] CCR method.
[c] ICP value.
[d] nominal value.
[e] CO-stripping.
[f] calculated by cm^2$_{Pt}$/cm^2$_{geo}$.

(*ca.* 7.1 nm). Besides, the charge of the double layer decreases from TiO$_2$-C (1825 μC cm^{-2}$_{geo}$) to Y:TiO$_2$-C (962 μC cm^{-2}$_{geo}$) samples. The possible reason for the lower current density in Pt/Y:TiO$_2$-C could be due to i the large particle size of Pt (19 nm), and/or ii the metal-semiconductor junction between Pt and Y:TiO$_2$ phases [44].

In order to compare the performance of the materials, the electrochemical active surface area (ECSA) calculated from H$_{upd}$ and CO-stripping (see detailed discussion in CO-stripping analysis) using Eq. (10) [14,43].

$$ECSA_n = \frac{1}{Q_{Pt}v} \left[\int_{E_0}^{E_f} j_n(E)\,\partial E - \int_{E_0}^{E_f} j_n^{dl}(E)\,\partial E \right] \tag{10}$$

where n = H$_{upd}$ or CO, j is the intensity current (μA), E is the potential (V), Q_{Pt} is the density charge for Platinum (210 or 420 μC cm^{-2}, respectively for H$_{upd}$ and CO), j^{dl} is the current of the double layer (μA) and v is the scan rate (Vs^{-1}).

The Table 2 summarizes the ECSA values for Pt/C, Pt/TiO$_2$-C, Pt/Y:TiO$_2$-C, compared with the references of Pt/TiO$_2$ (prepared via photo-deposition) and Pt/C (synthesized via carbonyl chemical route [45]). From Table 2, it is clear that the samples prepared via photo-deposition method have ECSA and roughness values lower than that generated via carbonyl chemical route (CCR). An interesting aspect is, however, found in Pt/TiO$_2$, where the ratio of ECSA$_{CO}$/ECSA$_H$ is equal to 2, indicating larger amount of adsorbed CO molecules in contrast to adsorbed protons onto Pt surface. This phenomenon, earlier observed, was explained as proton adsorption occurring on both TiO$_2$ surface and Pt surface [46,47], whereas the CO molecule adsorption is preferentially adsorbed at Pt surface.

3.3.3. CO-stripping analysis

The CO stripping voltammograms for Pt/C, Pt/TiO$_2$-C and Pt/Y:TiO$_2$-C catalysts, prepared via photo-deposition (PD), are contrasted in Fig. 7. In order to study the SMSI effect in detail [48], the CO-stripping voltammograms for Pt NPs, supported on TiO$_2$ via PD and carbon black synthesized via CCR, are also depicted in the figure. The CO oxidation peak at 0.64 V/RHE on Pt/TiO$_2$ (PD) catalyst is ascribed to the SMSI of Pt and oxide (Pt/oxide) [33]. The CO oxidized at 0.73 V/RHE on Pt/C (CCR) can be also attributed to the interaction between Pt and disordered domain sp^3 of carbon (C-sp^3) [45].

For Pt/C (PD), we can observe two main CO-oxidation peaks at *ca.* 0.66 and 0.73 V/RHE, respectively. The first peak can be attributed to CO oxidation on the Pt NPs supported on graphitic domains of carbon, suggesting a strong interaction via hybridization of d orbitals of Pt with carbon sp^2 domains (Pt/C-sp^2) [33]. The wave centered at *ca.* 0.73 V/RHE, corresponding to the main peak of Pt/C (CCR) sample, should be related to CO oxidation at Pt sites interacting with disordered carbon, namely, C-sp^3 [45]. Besides, it can be seen that the first CO-oxidation peak (*ca.* 0.66 V/REH) is more prominent than the second one (*ca.* 0.73 V/RHE), indicating that Pt NPs are deposited more selectively onto C-sp^2 domains. On the other hand, a shoulder located at 0.4 and 0.68 V/RHE in Pt/C (PD) and Pt/C (CCR), might be
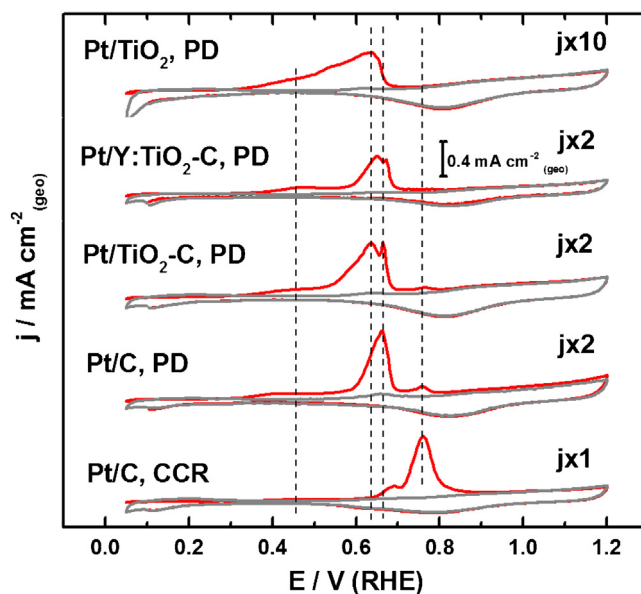

Fig. 7. CO-stripping characteristic in acid conditions (0.1 M HClO$_4$) for Pt-based nanoparticles supported on XC-72, TiO$_2$-C and Y:TiO$_2$-C composite. The dashed lines indicate different interactions effect.

associated to Pt NPs agglomeration [49,50] as confirmed by *p*XRD and TEM analysis, i.e. increased particle size in Pt/C (PD) in TEM, and a bimodal behavior on Pt/C (CCR) in *p*XRD.

For Pt/TiO$_2$-C, we observe the interaction attributable to Pt/Oxide [33,34] (*cf.* peak at 0.64 V/RHE) and Pt/C-sp^2 (*cf.* peak at 0.66 V/RHE), and to Pt/C-sp^3 (*cf.* peak at 0.73 V/RHE). Summing up, these facts assess that the PD process allows the selective deposition of Pt NPs onto oxide sites and ordered domains of carbon. The hybridization belonging to Pt/C-sp^3 is not observed on Pt/Y:TiO$_2$-C (PD) sample, indicating an unique effect of Y:TiO$_2$-C towards photo-deposition of Pt NPs. This phenomenon, as discussed below, affects positively the ORR process of Pt NPs.

3.4. ORR process

The ORR polarization curves at 900 rpm for all the PD generated catalysts are shown in Fig. 8A. It can be found that the half-wave potentials for the catalysts are rather close at *ca.* 0.9 V/RHE. The corresponding Tafel plot is shown in Fig. 8B. These results demonstrate that the mechanism of ORR is similar for all electrocatalyst investigated herein, since the Tafel slope is *ca.* 69, 63 and 62 mV dec^{-1} for Pt/C, Pt/TiO$_2$-C and Pt/Y:TiO$_2$-C, respectively. Therefore, the specific activity (SA), and mass activity (MA) of all electrocatalysts at 0.9 V/RHE was calculated from, Eqs. (11) and (12) [51].

$$SA = j_k\varphi^{-1} \tag{11}$$

$$MA = SA\frac{\varphi}{L_{Pt}} \tag{12}$$

where j_k is the current density normalized by the geometric area, φ is the roughness (cm^2$_{real}$/cm^2$_{geo}$) and L_{Pt} is the Pt mass loading per geometric surface area (Pt mass from ICP/cm^{-2}$_{geo}$). From Fig. 8C, we can observe that the specific activity (SA) follows the sequence: Pt/Y:TiO$_2$-C > Pt/C > Pt/TiO$_2$-C, opposite to that of ECSA (m^2 g^{-1}$_{Pt}$), see Table 2. In fact, the ECSA (m^2 g^{-1}$_{Pt}$) value in Pt/TiO$_2$-C was 42 m^{2}g^{-1}$_{Pt}$, higher than that in Pt/C (36 m^{2}g^{-1}$_{Pt}$) and in Pt/Y:TiO$_2$-C (21 m^{2}g^{-1}$_{Pt}$). However, the trend in the mass activity (MA) shows the same tendency to that of ECSA (m^2 g^{-1}$_{Pt}$). The kinetic current normalized by real surface area of Pt (deduced from either from H$_{upd}$ and/or CO stripping), shows that the ORR is not related to the dispersion of Pt NPs [5], but to another process related to the inter-
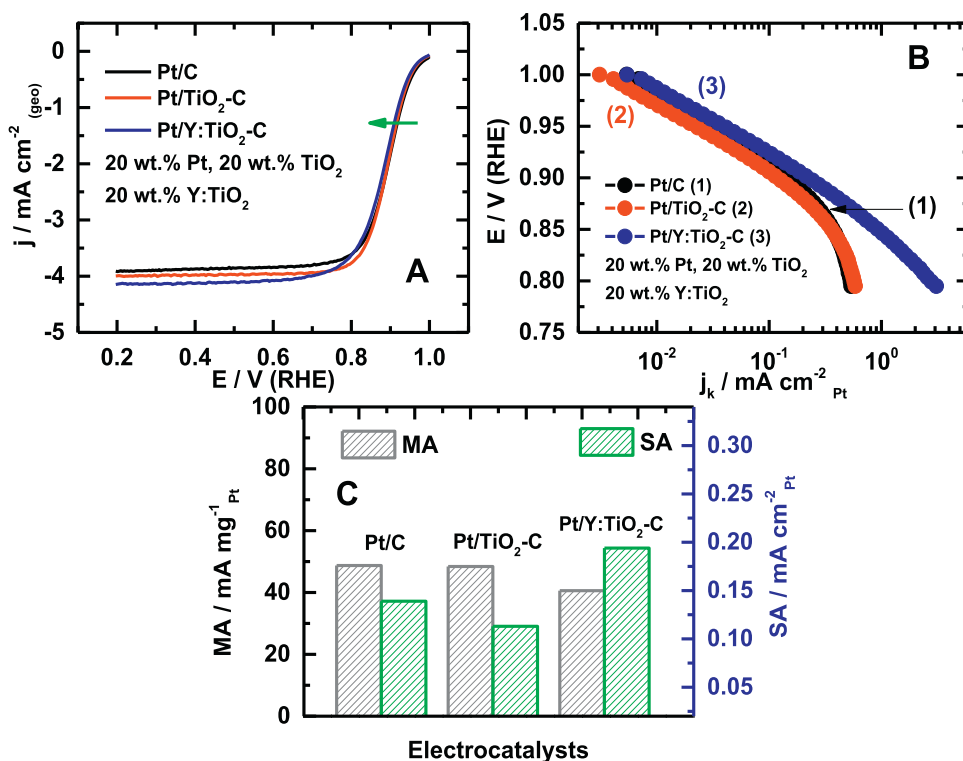
Fig. 8. (A) ORR in saturated oxygen-electrolyte at 900 rpm in 0.1 M $HClO_4$ at 5 mVs-1, (B) Tafel plots and (C) Mass activity, specific activity for Pt/C, Pt/TiO_2-C and $Pt/Y:TiO_2$-C at 25 °C by PD method. The mass of Pt was evaluated from the ICP data.

action of the catalytic particles with the support, probed by the CO-stripping experiments.

The accelerated stability test (AST) at room temperature was performed. Fig. 9 shows the evolution of ECSA (remaining H_{upd}) and kinetic current (remaining j_k at 0.9 V/RHE), after cycling in two different potential regions, from *ca.* 0.6 to 1.0 V/RHE (R1) and from *ca.* 0.6 to 1.2 V/RHE (R2). According to the literature, four different degradation mechanisms (*i.e.* Ostwald ripening, agglomeration, detachment and carbon corrosion) can be found in fuel cell electrocatalyst at start-stop conditions [52]. Based on our previous experience [2] the intrinsic agglomeration of Pt NPs could be reduced during AST due to enhanced interaction with the support.

Detachment and carbon corrosion might be avoided using the R1 condition; *cf.* support corrosion curves are shown in inset of Fig. 5. One can observe in Fig. 9 that the ECSA evolution for all the catalysts is almost the same using the procedure R1. The remaining j_k on Pt/C is slightly higher than those of $Pt/Y:TiO_2$-C and Pt/TiO_2-C. Recently, Meier et al. reported that the catalyst degradation is caused by Ostwald ripening when the average particle size is below 6 nm [52]. However, this particle/crystallite size effect using R1 procedure should be negligible, because only about 20% of particles diameter is below 6 nm in Pt/TiO_2-C and no particle with diameter lower than 6 nm can be found in Pt/C and $Pt/Y:TiO_2$-C samples (*cf.* Fig. 1). The most plausible explanation for such trend of j_k should be related to the strain effect, discussed in XRD analysis section.

On Vulcan (XC-72), TiO_2-C and $Y:TiO_2$-C supports, the corrosion of carbon can be observed at potential higher than 1.0 V/RHE (*cf.* Fig. 5 insets). Therefore, in AST using procedure R2, one can observe the same trend for both the remaining ECSA and j_k, namely, $Pt/Y:TiO_2$-C > Pt/TiO_2-C > Pt/C. Bearing in mind the CO-stripping results (*cf.* Fig. 7), Pt NPs could be deposited onto three domains: onto oxide sites, onto C-sp^2, and onto C-sp^3 domains. When the catalysts are cycled to a potential as high as 1.2 V/RHE, Pt NPs could be largely detached because of carbon corrosion, as occurs in Pt/C sample. However, the interaction (SMSI effect) between Pt and oxide

prevents such a phenomenon in Pt/TiO_2-C and $Pt/Y:TiO_2$-C. Taking CO-stripping into account, one can assess that, in $Pt/Y:TiO_2$-C sample, Pt NPs are deposited preferentially onto oxides sites and graphitic domains rather than on disordered domains of carbon, with respect to Pt/TiO_2-C sample, favoring the ORR stability. These facts, indeed, reveal a positive effect of Y-dopant in TiO_2 on Pt NPs.

4. Conclusion

Pt NPs supported on XC-72, TiO_2-C and $Y:TiO_2$-C was synthesized *via* photo-deposition route and their ORR activity and stability in acid conditions were investigated. Based on the analysis of XRD patterns, the Pt (*fcc*) and TiO_2 (Anatase) phases were identified in Pt/TiO_2-C and $Pt/Y:TiO_2$-C. TEM and CO-stripping analyses revealed that, by photo-deposition, the Pt NPs are mainly deposited on oxide and some NPs onto carbon phase in both Pt/TiO_2-C and $Pt/Y:TiO_2$-C sample. The stability of the support is due to the modification of carbon with $Y:TiO_2$ as confirmed by the electrical conductivity, cyclic voltammetry and stability measurements. This work provides evidence for the effect of Y as dopant on photo-electrochemical property and electrical conductivity of TiO_2. Surface electrochemistry (CV and CO-stripping) also revealed the difference in the interaction (SMSI) between $Pt/Y:TiO_2$-C and Pt/TiO_2-C sample. ORR kinetics and stability tests confirm the positive effect of $Y:TiO_2$/C towards Pt active centers. Therefore, the composite based on carbon black with Y-doped TiO_2 is a promising advanced support material to improve the electrocatalytic performance of Pt centre towards the oxygen reduction reaction.
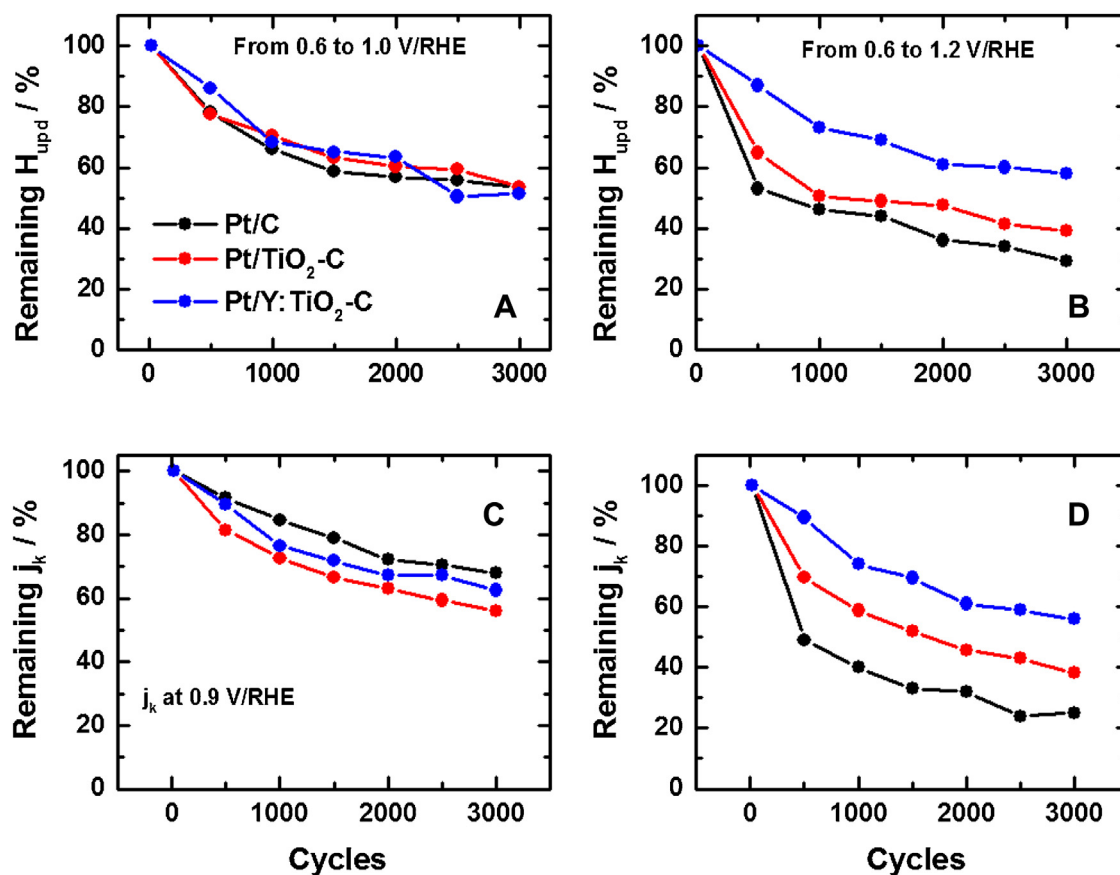
Fig. 9. Normalized ECSA loss and kinetic current under potential cycling from 0.6 to 1.0 V/RHE (A) and from 0.6 to 1.2 V/RHE (B) in 0.1 M HClO$_4$ at 25 °C for Pt/C, Pt/TiO$_2$-C and Pt/Y:TiO$_2$-C.

Appendix A. Supplementary data

Supplementary data associated with this article can be found, in the online version, at http://dx.doi.org/10.1016/j.apcatb.2016.01.030.

References

[1] N. Alonso-Vante, Carbonyl tailored electrocatalysts, Fuel Cells 6 (2006) 182–189.
[2] N. Alonso-Vante, Platinum and non-platinum nanomaterials for the molecular oxygen reduction reaction, ChemPhysChem 11 (2010) 2732–2744.
[3] E. Antolini, Carbon supports for low-temperature fuel cell catalysts, Appl. Catal. B: Environ. 88 (2009) 1–24.
[4] K. Wipke, S. Sprik, J. Kurtz, T. Ramsden, C. Ainscough, G. Saur, Controlled hydrogen fleet and infrastructure analysis, 2011 DOE Annual Merit Review and Peer Evaluation Meeting (2011) 1–31.
[5] Y. Luo, A. Habrioux, L. Calvillo, G. Granozzi, N. Alonso-Vante, Yttrium oxide/gadolinium oxide-modified platinum nanoparticles as cathodes for the oxygen reduction reaction, ChemPhysChem 15 (2014) 2136–2144.
[6] C.V. Rao, B. Viswanathan, ORR activity and direct ethanol fuel cell performance of carbon-supported Pt-M (M = Fe, Co, and Cr) alloys prepared by polyol reduction method, J. Phys. Chem. C 113 (2009) 18907–18913.
[7] G. Fu, K. Wu, J. Lin, Y. Tang, Y. Chen, Y. Zhou, et al., One-pot water-based synthesis of Pt-Pd alloy nanoflowers and their superior electrocatalytic activity for the oxygen reduction reaction and remarkable methanol-Tolerant ability in acid media, J. Phys. Chem. C 117 (2013) 9826–9834.
[8] Y. Holade, N. Sahin, K. Servat, T. Napporn, K. Kokoh, Recent advances in carbon supported metal nanoparticles preparation for oxygen reduction reaction in low temperature fuel cells, Catalysts 5 (2015) 310–348.
[9] X. Yu, S. Ye, Recent advances in activity and durability enhancement of Pt/C catalytic cathode in PEMFC, J. Power Sources 172 (2007) 133–144.
[10] A. Manzo-Robledo, A.-C. Boucher, E. Pastor, N. Alonso-Vante, Electro-oxidation of carbon monoxide and methanol on carbon-supported Pt ± Sn nanoparticles: a DEMS study, Fuel Cells 2 (2002) 109–116.
[11] S. Zhao, A.E. Wangstrom, Y. Liu, W.A. Rigdon, W.E. Mustain, Stability and activity of Pt/ITO electrocatalyst for oxygen reduction reaction in alkaline media, Electrochim. Acta 157 (2015) 175–182.
[12] L. Timperman, Y.J. Feng, W. Vogel, N. Alonso-Vante, Substrate effect on oxygen reduction electrocatalysis, Electrochim. Acta 55 (2010) 7558–7563.
[13] W. Vogel, L. Timperman, N. Alonso-vante, Probing metal substrate interaction of Pt nanoparticles: structural XRD analysis and oxygen reduction reaction, Appl. Catal. A: Gen. 377 (2010) 167–173.
[14] L. Timperman, A. Lewera, W. Vogel, N. Alonso-Vante, Nanostructured platinum becomes alloyed at oxide-composite substrate, Electrochem. Commun. 12 (2010) 1772–1775.
[15] K. Rajeshwar, C. Janaky, W.-Y. Lin, D.A. Roberts, W. Wampler, Photocatalytically prepared metal nanocluster-oxide semiconductor-carbon nanocomposite electrodes for driving multielectron transfer, J. Phys. Chem Lett. 4 (2013) 3468–3478.
[16] A. Rabis, P. Rodriguez, T.J. Schmidt, Electrocatalysis for polymer electrolyte fuel cells: recent achievements and future challenges, ACS Catal. 2 (2012) 864–890.
[17] R. Li, F. Zhang, D. Wang, J. Yang, M. Li, J. Zhu, et al., Spatial separation of photogenerated electrons and holes among {010} and {110} crystal facets of BiVO$_4$, Nat. Commun. 4 (2013) 1432–1439.
[18] J. Ma, E. Valenzuela, A.S. Gago, J. Rousseau, A. Habrioux, N. Alonso-Vante, Photohole trapping induced platinum cluster nucleation on the surface of TiO$_2$ nanoparticles, J. Phys. Chem. C 118 (2014) 1111–1117.
[19] S. Shironita, K. Mori, T. Shimizu, T. Ohmichi, N. Mimura, H. Yamashita, Preparation of nano-sized platinum metal catalyst using photo-assisted deposition method on mesoporous silica including single-site photocatalyst, Appl. Surf. Sci. 254 (2008) 7604–7607.
[20] K. Mori, T. Araki, S. Shironita, J. Sonoda, H. Yamashita, Supported Pd and PdAu nanoparticles on Ti-MCM-41 prepared by a photo-assisted deposition method as efficient catalysts for direct synthesis of H$_2$O$_2$ from H$_2$ and O$_2$, Catal. Lett. 131 (2009) 337–343.
[21] R. Daghrir, P. Drogui, D. Robert, Modified TiO$_2$ for environmental photocatalytic applications: a review, Ind. Eng. Chem. Res. 52 (2013) 3581–3599.

[22] Y. Bai, I. Mora-Seró, F. De Angelis, J. Bisquert, P. Wang, Titanium dioxide nanomaterials for photovoltaic applications, Chem. Rev. 114 (2014) 10095–10130.

[23] A. Kumar, V. Ramani, Strong metal-support interactions enhance the activity and durability of platinum supported on tantalum-modified titanium dioxide electrocatalysts, ACS Catal. 4 (2014) 1516–1525.

[24] S. Mokrane-Soualah, A.S. Gago, A. Habrioux, N. Alonso-Vante, Mixed-oxide $Ti_{1-x}W_xO_2$ as support for (photo)-electrochemical processes, Appl. Catal. B: Environ. 147 (2014) 756–763.

[25] V.T.T. Ho, C.-J. Pan, J. Rick, B.-N. Su, B.-J. Hwang, Nanostructured $Ti_{0.7}Mo_{0.3}O_2$ support enhances electron transfer to Pt: high-performance catalyst for oxygen reduction reaction, J. Am. Chem. Soc. 133 (2011) 11716–11724.

[26] V.T.T. Ho, K. Chandrasekara Pillai, H.-L. Chou, C.-J. Pan, J. Rick, W.-N. Su, B.-J. Hwang, J.-F. Lee, H.-S. Sheu, W.-T. Chuang, Robust non-carbon $Ti_{0.7}Ru_{0.3}O_2$ support with co-catalytic functionality for Pt: enhances catalytic activity and durability for fuel cells, Energy Environ. Sci. 4 (2011) 4194–4200.

[27] S. Watanabe, X. Ma, C. Song, V. Pennsyl, Characterization of Structural and Surface Properties of Nanocrystalline TiO_2-CeO_2 Mixed Oxides by XRD, XPS, TPR, and TPD, J. Phys. Chem. C 113 (2009) 14249–14257.

[28] M. Khan, W. Cao, Preparation of Y-doped TiO_2 by hydrothermal method and investigation of its visible light photocatalytic activity by the degradation of methylene blue, J. Mol. Catal. A: Chem. 376 (2013) 71–77.

[29] J. Ma, A. Habrioux, N. Alonso-Vante, Enhanced HER and ORR behavior on photodeposited Pt nanoparticles onto oxide?carbon composite, J. Solid State Electrochem. 17 (2013) 1913–1921.

[30] Espinola, M. Pablo Mourente, S. Milton Roedel, A. Ribeiro Pinto, Electrical properties of carbons-resistance of powder materials, Carbon. 24 (1986) 337–341.

[31] W.D. Callister, D.G. Rethwisch, Materials Science and Engineering: An Introduction, 7th ed., John Wiley & Sons, United States of America, 2007, pp. 80–109.

[32] S.E. Haghighi, K. Janghorban, S. Izadi, Structural evolution of Fe–50 at.% Al powders during mechanical alloying and subsequent annealing processes, J. Alloys Compd. 495 (2010) 260–264.

[33] J. Ma, A. Habrioux, C. Morais, A. Lewera, W. Vogel, Y. Verde-Gómez, G. Ramos-Sanchez, P.B. Balbuena, N. Alonso-Vante, Spectroelectrochemical probing of the strong interaction between platinum nanoparticles and graphitic domains of carbon, ACS Catal. 3 (2013).

[34] A. Lewera, L. Timperman, A. Roguska, N. Alonso-Vante, Metal-support interactions between nanosized Pt and metal oxides (WO_3 and TiO_2) studied using X-ray photoelectron spectroscopy, J. Phys. Chem. C 115 (2011) 20153–20159.

[35] Y. Luo, J.M. Mora-hernández, L.A. Estudillo-Wong, E.M. Arce-estrada, N. Alonso-Vante, Nanostructured palladium tailored via carbonyl chemical route towards oxygen reduction reaction, Electrochim. Acta 173 (2015) 771–778.

[36] H. Zhang, X. Yu, J.A. McLeod, X. Sun, First-principles study of Cu-doping and oxygen vacancy effects on TiO_2 for water splitting, Chem. Phys. Lett. 612 (2014) 106–110.

[37] T. Berger, T. Lana-Villarreal, D. Monllor-Satoca, R. Gómez, An electrochemical study on the nature of trap states in nanocrystalline rutile thin flims, J. Phys. Chem. C 111 (2007) 9936–9942.

[38] T. Lana-Villarreal, Y. Mao, S.S. Wong, R. Gómez, Photoelectrochemical behaviour of anatase nanoporous films: effect of the nanoparticle organization, Nanoscale. 2 (2010) 1690–1698.

[39] H. Zhou, Y. Zhang, Electrochemically self-doped TiO_2 nanotube arrays for supercapacitors, J. Phys. Chem. C 118 (2014) 5626–5636.

[40] R. Beranek, (Photo) electrochemical methods for the determination of the band edge positions of TiO_2-based nanomaterials, Adv. Phys.Chem. 2011 (2011) 1–20.

[41] P. Trogadas, T.F. Fuller, P. Strasser, Carbon as catalyst and support for electrochemical energy conversion, Carbon 75 (2014) 5–42.

[42] A.T. Ezhil Vilian, S.-M. Chen, S. Piraman, The electrochemical synthesis of Pt particles on ZrO_2–ERGO modified electrodes with high electrocatalytic performance for methanol oxidation, New J. Chem. 39 (2015) 953–961.

[43] F.J. Vidal-Iglesias, R.M. Arán-Ais, J. Solla-Gullón, E. Herrero, J.M. Feliu, Electrochemical characterization of shape-controlled Pt nanoparticles in different supporting electrolytes, ACS Catal. 2 (2012) 901–910.

[44] S. Siracusano, A. Stassi, E. Modica, V. Baglio, A.S. Aricò, Preparation and characterisation of Ti oxide based catalyst supports for low temperature fuel cells, Int. J. Hydrogen Energy 38 (2013) 11600–11608.

[45] J. Ma, A. Habrioux, N. Guignard, N. Alonso-Vante, Functionalizing effect of increasingly graphitic carbon supports on carbon-supported and TiO_2-carbon composite-supported Pt nanoparticles, J. Phys. Chem. C 116 (2012) 21788–21794.

[46] L.A. Estudillo-Wong, E.M. Arce-Estrada, A. Manzo-Robledo, Interaction of NO during cathodic polarization at the interface of Pt-nanostructures supported on C and TiO_2-C, Electrochim. Acta 134 (2014) 100–106.

[47] A. Ghicov, H. Tsuchiya, R. Hahn, J.M. Macak, A.G. Muñoz, P. Schmuki, TiO_2 nanotubes: h$^+$ insertion and strong electrochromic effects, Electrochem. Commun. 8 (2006) 528–532.

[48] S.J. Tauster, S.C. Fung, R.L. Garten, Strong metal-support interactions. group 8 noble metals supported on TiO_2, J. Am. Chem. Soc. 4 (1978) 170–175.

[49] F. Maillard, M. Eikerling, O.V. Cherstiouk, S. Schreier, E. Savinova, U. Stimming, Size effects on reactivity of Pt nanoparticles in CO monolayer oxidation: the role of surface mobility, Faraday Discuss. 125 (2004) 357–377.

[50] A. López-Cudero, J. Solla-Gullón, E. Herrero, A. Aldaz, J.M. Feliu, CO electrooxidation on carbon supported platinum nanoparticles: effect of aggregation, J. Electroanal. Chem. 644 (2010) 117–126.

[51] K.J.J. Mayrhofer, D. Strmcnik, B.B. Blizanac, V. Stamenkovic, M. Arenz, N.M. Markovic, Measurement of oxygen reduction activities via the rotating disc electrode method: from Pt model surfaces to carbon-supported high surface area catalysts, Electrochim. Acta 53 (2008) 3181–3188.

[52] J.C. Meier, C. Galeano, I. Katsounaros, A.A. Topalov, A. Kostka, F. Schüth, et al., Degradation mechanisms of Pt/C fuel cell catalysts under simulated start-stop conditions, ACS Catal. 2 (2012) 832–843.